Advanced Materials Interfaces

www.advmatinterfaces.de

RESEARCH ARTICLE OPEN ACCESS

Designing Defect Structure and Interfacial Strain in an Epitaxial VN Bilayer Film by Tailoring N Concentration

Marcus Hans[1] | Damian M. Holzapfel[1] | Zhuo Chen[2] | Soheil Karimi Aghda[1] | Michal Fečík[1] | Daniel Primetzhofer[3] | Zaoli Zhang[2] | Jochen M. Schneider[1]

[1]Materials Chemistry, RWTH Aachen University, Aachen, Germany | [2]Erich Schmid Institute of Materials Science, Austrian Academy of Sciences, Leoben, Austria | [3]Department of Physics and Astronomy, Uppsala University, Uppsala, Sweden

Correspondence: Marcus Hans (hans@mch.rwth-aachen.de)

Received: 26 August 2025 | **Revised:** 6 December 2025 | **Accepted:** 24 December 2025

Keywords: atom probe tomography | frenkel pair | HiPIMS | transition metal nitride | transmission electron microscopy

ABSTRACT

A bilayer of $V_{0.49}N_{0.51}/V_{0.56}N_{0.44}$ has been grown epitaxially on MgO(001) by reactive high-power pulsed magnetron sputtering in an industrial-scale deposition system at a temperature of 400°C, and it is demonstrated that the defect structure and interfacial strain are governed by the N concentration. Based on the lattice mismatch between MgO and $V_{0.49}N_{0.51}$ with V vacancies, an interfacial strain of −2.3(1)% is expected. From ab initio calculations, X-ray diffraction, and transmission electron microscopy data, it is inferred that the $V_{0.49}N_{0.51}$ layer exhibits V vacancies, N Frenkel pairs, and a high dislocation density of ≈0.20 nm^{-2}, causing an interfacial strain of −1.4(5)% at the MgO/$V_{0.49}N_{0.51}$ interface. The phase formation of understoichiometric $V_{0.56}N_{0.44}$ is governed by N vacancy formation, while the dislocation density is reduced to ≈0.04 nm^{-2} at the $V_{0.49}N_{0.51}/V_{0.56}N_{0.44}$ interface and to < 0.01 nm^{-2} within $V_{0.56}N_{0.44}$ at a distance of ≈35 nm from the interface. Based on ab initio calculations, a strain of −1.7(6)% is predicted at the $V_{0.49}N_{0.51}/V_{0.56}N_{0.44}$ interface in very good agreement with the experimentally obtained value of −1.6(8)%. It is evident that control of the N concentration allows for the design of layered architectures with well-defined strained interfaces and tailored defect structures.

1 | Introduction

Transition metal nitrides are widely used as protective, functional, or decorative thin films due to the mixture of covalent, ionic, and metallic bonds [1]. Well-studied examples are TiN as well as VN, which exhibit a face-centered cubic crystal structure (NaCl prototype, space group $Fm\bar{3}m$). While TiN synthesis consisted of annealing transition metal oxides at temperatures well above 1200°C in N-containing atmosphere 100 years ago [2], physical vapor deposition processes became popular in the 1970s [3]. The first stoichiometric single-crystalline TiN thin films were synthesized in 1985, pioneering epitaxial growth on MgO substrates at temperatures > 525°C with dc magnetron sputtering [4].

The mechanical properties of such epitaxially grown films with single-crystalline microstructure are governed by the composition. Reduction of N from 50 to 40 at.% in TiN caused enhancement of the hardness from 20 ± 2 to 30 ± 2 GPa, while the elastic modulus was lowered from 430 ± 30 to 330 ± 20 GPa [5]. The reduction of elastic modulus can be understood based on the occupation of metallic bonding states in TiN, caused by the presence of N vacancies [6]. Vacancy hardening was suggested to originate from variations in the local bond environment as well as limited dislocation mobility [5]. Recently, N vacancy pinning effects at the dislocation core were predicted [7].

In contrast to TiN, enhancement of both hardness as well as elastic modulus was found in understoichiometric VN. N

This is an open access article under the terms of the Creative Commons Attribution License, which permits use, distribution and reproduction in any medium, provided the original work is properly cited.

© 2026 The Author(s). *Advanced Materials Interfaces* published by Wiley-VCH GmbH

concentrations of 50 and 44 at.% resulted in hardness values of 14 ± 1 and 17 ± 1 GPa, respectively [8], and the elastic modulus increased from 400 ± 25 to 444 ± 24 GPa, when the N content was reduced from 49 ± 1 to 44 ± 1 at.% [9]. This anomalous increase in elastic modulus was explained by the elastic anisotropy and bond strengthening in VN, since vacancy-induced softening, predicted for the [001] direction, is overcompensated by strengthening along [011] and [111] directions [9]. Moreover, the fracture toughness has been qualitatively assessed via nanoindentation, and it was shown that understoichiometric $V_{0.56}N_{0.44}$ is more resistant to fracture than stoichiometric $V_{0.50}N_{0.50}$ [8].

Epitaxial growth has been utilized for the synthesis of single-crystalline superlattices with strained interfaces due to the lattice mismatch of different transition metal nitrides. For TiN/VN superlattices with a bilayer period of ≈5.2 nm (and individual layer thicknesses of ≈2.6 nm), a hardness value > 50 GPa has been reported, while single-crystalline monolithic TiN and VN films had a hardness of < 25 GPa [10]. Recent atomic-scale investigations of single-crystalline TiN/AlN superlattices revealed that strengthening is governed by the accumulation and crossing of dislocations at the interfaces [11].

Motivated by the strengthening effect in superlattices described above, many additional studies were conducted with combinations of different transition metal nitrides (and varying stoichiometries) such as ZrN/AlN [12], TiN/NbN [13], CrN/AlN [14], TiN/CrN [15], NbN/MoN [16], TiN/WN [17], and MoN/TaN [18]. However, the design of layered nitrides based on only one transition metal and varying N concentration has been overlooked so far. In case of a Cr/CrN architecture, a 20 nm thin, compressively stressed Cr_2N transition layer was identified [19]. It can be expected that control of the chemical composition enables the materials design of layered nitrides with variations in the defect structure, which in turn affect the materials properties. Moreover, separate contributions of gradients from variations of the atomic distance as well as the composition might be expected at the interfaces [20]. The employment of only one transition metal is chemically simple and therefore, from a recycling point of view, also more sustainable than combining different transition metals [21].

In the present work, an epitaxial VN(001) bilayer film was grown on MgO(001), using reactive high-power pulsed magnetron sputtering (HPPMS) [22] in an industrial-scale deposition system. The bilayer consists of ≈45 nm overstoichiometric $V_{0.49}N_{0.51}$ as well as ≈110 nm understoichiometric $V_{0.56}N_{0.44}$. From ab initio calculations, X-ray diffraction (XRD), and transmission electron microscopy (TEM), it is inferred that the $V_{0.49}N_{0.51}$ layer exhibits V vacancies, N Frenkel pairs, and a high dislocation density, while the density of dislocations in the $V_{0.56}N_{0.44}$ layer with N vacancies is reduced by two orders of magnitude. Based on these results, it is evident that control of the N concentration allows for the design of layered architectures with well-defined strained interfaces and tailored defect structures.

2 | Results and Discussion

2.1 | Reactive Synthesis of the Bilayer

VN bilayer films were grown onto MgO(001) and glassy C at 400°C in an industrial-scale deposition system using reactive HPPMS. In order to tune the stoichiometry, different gas supply systems of N_2 were employed, as schematically shown in Figure 1. The first layer was intended to be overstoichiometric (N concentration > 50 at.%), and N_2 gas was provided through the central gas inlet of the deposition system, Figure 1a. The second layer was intended to be understoichiometric (N concentration < 50 at.%), and N_2 was introduced through a different inlet (referred to as gas shower in the following) placed at one end of the V sputtering target, Figure 1b [23].

Representative waveforms of target voltage and current during HPPMS discharges are displayed in Figure 1c and Figure 1d, respectively. The voltages during pulses at the V sputtering target were −655 and −620 V, while peak target currents were 198 and 200 A, respectively. Consequently, the peak target powers were ≈130 and ≈124 kW, while the peak target power densities were 295 and 282 W cm^{-2}. Despite very similar power values, the deposition rate during growth with the gas shower was 3.1 Å s^{-1} and, thus, ≈29% higher compared to the deposition rate of 2.4 Å s^{-1} in the case of employing the central gas inlet. Deposition rates during reactive sputtering are significantly influenced by the metal nitride compound, which is formed at the target surface [24]. The partial pressure of N_2 gas was with 0.02 Pa, substantially smaller for the gas shower setup, compared to 0.10 Pa for the central gas inlet. Consequently, employment of a local N_2 gas inlet exhibits tremendous potential for savings of materials and energy, as the N_2 consumption was reduced by 80% and the deposition rate increased by 29%.

2.2 | VN Bilayer Composition and Compositional Gradient of $V_{0.49}N_{0.51}/V_{0.56}N_{0.44}$ Interface

The chemical composition of the films, synthesized on glassy C, was studied by Rutherford backscattering spectrometry (RBS), and the overstoichiometric layer exhibited a N concentration of 51 ± 2 at.%, independent of the position of the substrates on the holder. The compositional gradient in the second layer, induced by the N_2 supply from the gas shower, ranged from 50 ± 1 to 44 ± 1 at.% at distances from the gas shower inlet of ≈8 to ≈20 cm, respectively. The RBS spectrum of the VN bilayer film with the largest differences in N concentration is presented in Figure 2, and the experimental data are in very good agreement with a simulation of $V_{0.49}N_{0.51}$ for the overstoichiometric layer and $V_{0.56}N_{0.44}$ for the understoichiometric layer. This variation of the chemical composition is also detected in the V signal, but not discernible due to the logarithmic scale. In addition, O and Na impurities were identified in the glassy C substrate. O impurities within the bilayer were analyzed by time-of-flight elastic recoil detection analysis, and the O content decreased rapidly from ≈20 at.% at the surface to < 0.4 at.% within the first ≈10 nm depth from the surface. All of the following analyses pertain to this $V_{0.49}N_{0.51}/V_{0.56}N_{0.44}$ bilayer.

The compositional gradient at the $V_{0.49}N_{0.51}/V_{0.56}N_{0.44}$ interface was studied spatially-resolved at the nanometer scale using atom probe tomography (APT), Figure 3. An atom probe specimen was prepared from the VN bilayer, grown on MgO(001), and the reconstructions of V and N atomic positions are shown in Figure 3a,b, respectively. A higher N content in the $V_{0.49}N_{0.51}$ layer is emphasized by the overlay of both species, Figure 3c,

21967350, 0, Downloaded from https://advanced.onlinelibrary.wiley.com/doi/10.1002/admi.202500774 by Universitatsbibliothek RWTH Aachen University, Wiley Online Library on [12/01/2026]. See the Terms and Conditions (https://onlinelibrary.wiley.com/terms-and-conditions) on Wiley Online Library for rules of use; OA articles are governed by the applicable Creative Commons License

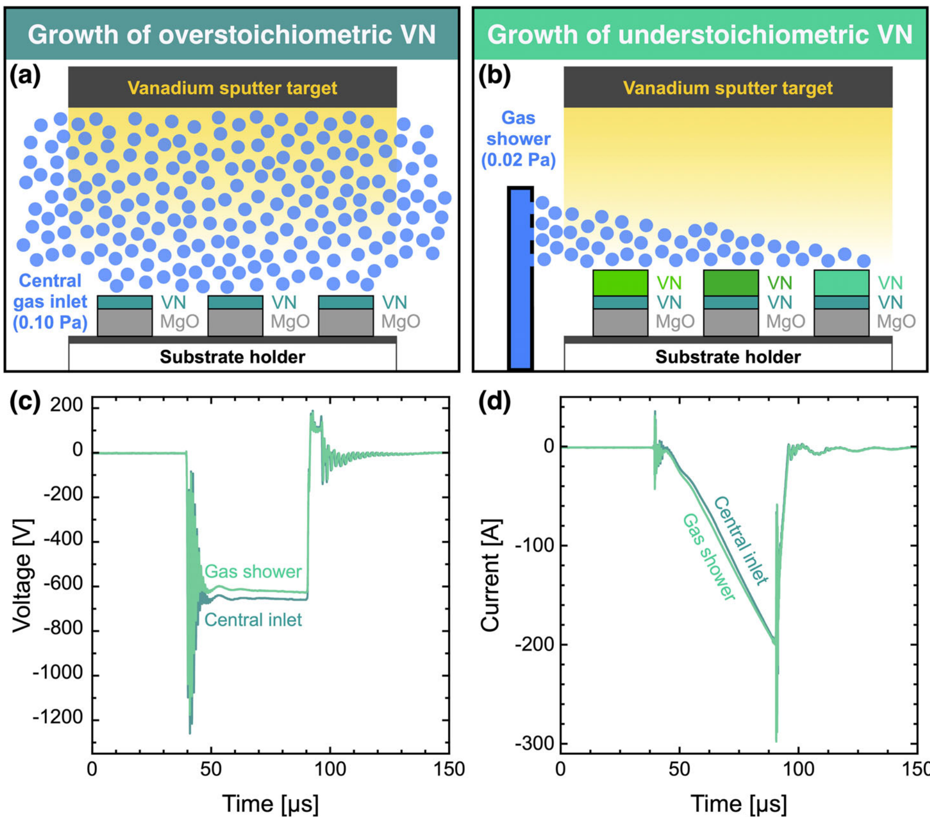

FIGURE 1 | Schematic representation of the synthesis strategy. (a) Homogeneous growth of the overstoichiometric layer using the central gas inlet. (b) Growth of the understoichiometric layer using an inlet placed at one end of the sputtering target (gas shower), which results in a composition gradient along the substrate holder [23]. (c) Target voltage and (d) target current waveforms recorded during discharges using the central gas inlet as well as the gas shower.

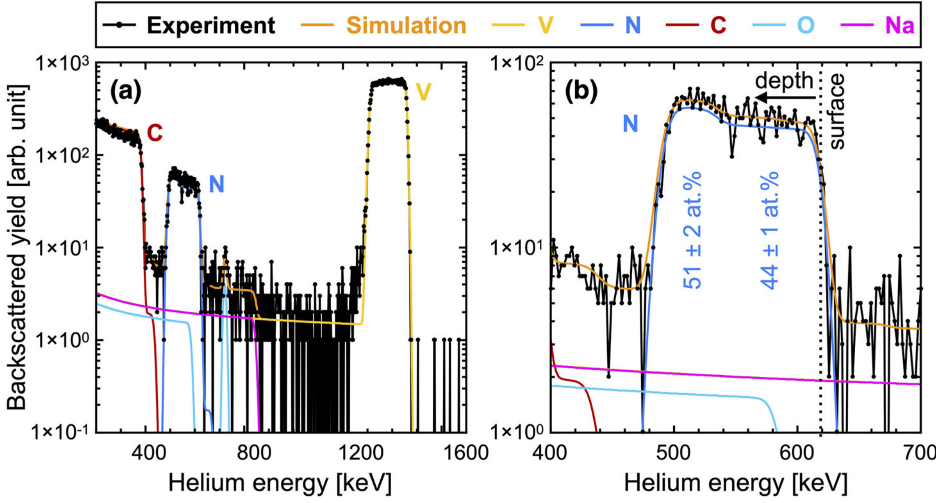

FIGURE 2 | Rutherford backscattering spectrum of the VN bilayer, grown on glassy C. (a) Overview with experimental data shown in black, while simulations for C, N, V, O, and Na are red, blue, gold, cyan, and magenta, respectively, while the total simulation fit is represented in orange. (b) Magnification of the N signal.

and the distance of 0 nm corresponds to the $V_{0.49}N_{0.51}/V_{0.56}N_{0.44}$ interface. The composition profile in Figure 3d is extracted from the cylindrical region, indicated in Figure 3c. While a constant N content of 48 ± 1 at.% is detected in the $V_{0.49}N_{0.51}$ layer, a steep decrease to 45 ± 1 at.% can be observed at the interface within a distance of ≈10 nm. The measured N content of the $V_{0.56}N_{0.44}$ layer exhibits a further decrease to 43 ± 1 at.%. Hence, the N reduction of 5 ± 1 at.%, measured with APT, is consistent with the 7 ± 2 at.% reduction, obtained from RBS.

Comparing the quantitative APT data to the composition from RBS, an underestimation of the N content up to 3 at.% is

21967350, 0, Downloaded from https://advanced.onlinelibrary.wiley.com/doi/10.1002/admi.202500774 by Universitatsbibliothek RWTH Aachen University, Wiley Online Library on [12/01/2026]. See the Terms and Conditions (https://onlinelibrary.wiley.com/terms-and-conditions) on Wiley Online Library for rules of use; OA articles are governed by the applicable Creative Commons License

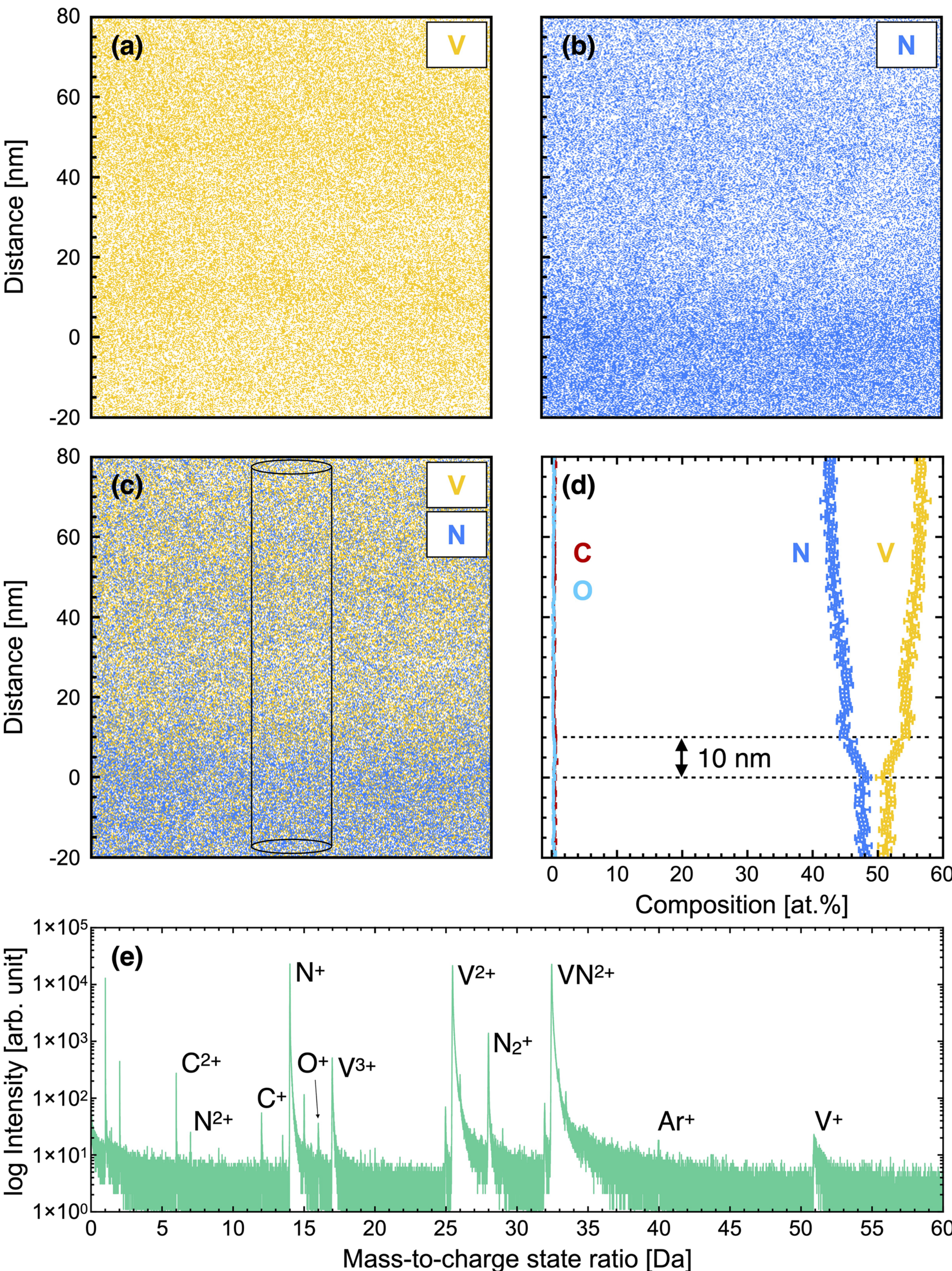

FIGURE 3 | Atom probe analysis of the $V_{0.49}N_{0.51}/V_{0.56}N_{0.44}$ interface. (a) Reconstruction of atomic positions of V. (b) Reconstruction of atomic positions of N. (c) Overlay of atomic positions of V (gold) and N (blue). The horizontal distance scale in panels (a–c) is identical to the vertical distance scale and not shown to enhance readability. (d) Composition profile from the cylindrical region (cylinder diameter of 20 nm), which is indicated in (c). The distance of 0 nm corresponds to the $V_{0.49}N_{0.51}/V_{0.56}N_{0.44}$ interface. (e) Mass spectrum.

21967350, 0, Downloaded from https://advanced.onlinelibrary.wiley.com/doi/10.1002/admi.202500774 by Universitatsbibliothek RWTH Aachen University, Wiley Online Library on [12/01/2026]. See the Terms and Conditions (https://onlinelibrary.wiley.com/terms-and-conditions) on Wiley Online Library for rules of use; OA articles are governed by the applicable Creative Commons License

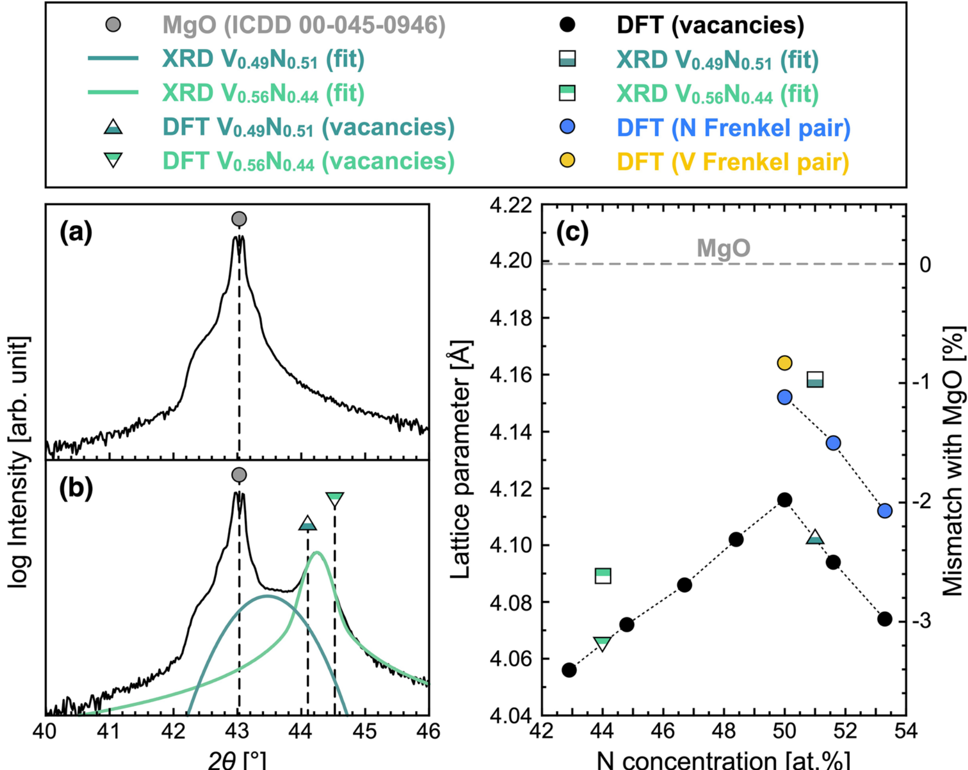

FIGURE 4 | Phase formation of the VN bilayer. (a) Diffractogram of the MgO(001) substrate and (b) of the VN bilayer, grown on MgO(001). (c) Evolution of lattice parameters (left axis) and the relative lattice mismatch with respect to MgO (right axis) as a function of N concentration, predicted by ab initio calculations (circles and triangles) and measured experimentally (squares). Configurations with vacancies only are represented by solid black circles, and triangles are interpolated values, while the golden and blue circles correspond to configurations with vacancies as well as V and N Frenkel pairs, respectively. Dashed lines are intended as a guide for the eye. Experimental lattice parameters for $V_{0.49}N_{0.51}$ and $V_{0.56}N_{0.44}$ are shown as half-filled squares and were obtained by application of Pseudo-Voigt fitting functions to XRD data in (b). The reference line of MgO is from the International Centre for Diffraction Data (ICDD, 00-045-0946), and reference lines of $V_{0.49}N_{0.51}$ and $V_{0.56}N_{0.44}$ in (b) are from interpolation of DFT data with vacancies only (triangles) in (c).

obvious. This discrepancy can be understood by dissociation of N-containing molecular ions, causing the formation of neutral fragments [25]. The mass spectrum is shown in Figure 3e, and dissociation of N_2^+ (at 28 Da) as well as VN^{2+} (at 32.5 Da) is likely to result in the formation of neutral N fragments, which cannot be detected. Furthermore, O and C impurities with average contents < 0.3 at.% can be observed without any dependence from the individual $V_{0.49}N_{0.51}$ and $V_{0.56}N_{0.44}$ layers or from the $V_{0.49}N_{0.51}/V_{0.56}N_{0.44}$ interface.

2.3 | Formation of Vacancies and Frenkel Pairs

Diffractograms of the uncoated MgO(001) substrate together with the VN bilayer, grown on MgO(001), as well as experimental and predicted lattice parameters, based on ab initio calculations, are presented in Figure 4. The peak from the MgO substrate is in excellent agreement with the reference line at $2\theta = 43.03°$, Figure 4a, corresponding to a lattice parameter of 4.199 Å. The diffraction signal from the VN bilayer contains contributions of $V_{0.49}N_{0.51}$ and $V_{0.56}N_{0.44}$ as revealed by the peak deconvolution, Figure 4b.

The $V_{0.49}N_{0.51}$ layer exhibits an experimental lattice parameter of 4.159 Å, derived from the position of the deconvoluted peak at $2\theta = 43.47°$ (mismatch of -0.9(5)% with respect to the MgO substrate). Considering only the incorporation of V vacancies in $V_{0.49}N_{0.51}$, a lattice parameter of 4.102 Å is predicted from density functional theory (DFT) data (mismatch of −2.3(1)% with respect to the MgO substrate), Figure 4c. Hence, the predicted lattice parameter of 4.102 Å, based on V vacancies only, exhibits a deviation of −1.3(7)% from the experimental lattice parameter of 4.159 Å. However, when the formation of an N Frenkel pair is considered in addition to two V vacancies (Frenkel pair concentration of 1.6%), DFT calculations yield an increased average lattice parameter of 4.138 Å (−1.4(5)% mismatch with MgO) compared to the prediction based on V vacancies only. The predicted lattice parameter of 4.138 Å for an N Frenkel pair and two V vacancies is in very good agreement with the experimental lattice parameter of 4.159 Å for $V_{0.49}N_{0.51}$, since the deviation is < 0.6%.

The formation energy of Frenkel pairs was obtained by comparing the total energy of a Frenkel pair-containing configuration with a perfect lattice (stoichiometric $V_{32}N_{32}$) or a lattice with V vacancies (overstoichiometric $V_{30}N_{32}$ and $V_{28}N_{32}$) counterpart. For stoichiometric $V_{32}N_{32}$, the formation energies of V and N Frenkel pairs are in the ranges of 4.6–4.7 and 4.5–4.7 eV, respectively. Despite the positive formation energies, the recombination of such Frenkel pairs, formed during ion bombardment [26], is kinetically constrained. However, in the case of overstoichiometric $V_{30}N_{32}$ and

21967350, 0, Downloaded from https://advanced.onlinelibrary.wiley.com/doi/10.1002/admi.202500774 by Universitatsbibliothek RWTH Aachen University, Wiley Online Library on [12/01/2026]. See the Terms and Conditions (https://onlinelibrary.wiley.com/terms-and-conditions) on Wiley Online Library for rules of use; OA articles are governed by the applicable Creative Commons License

$V_{28}N_{32}$ supercells, V Frenkel pairs recombine spontaneously. In contrast, N Frenkel pairs, which were found to persist in $V_{32}N_{32}$, remain also persistent in overstoichiometric systems, while the formation energies are increased to 4.8–5.0 and 5.8–5.9 eV in $V_{30}N_{32}$ and $V_{28}N_{32}$ cells, respectively. These formation energies of Frenkel pairs in VN are lower than in $V_{0.5}Al_{0.5}N$, which were 7.9 eV for V Frenkel pairs and 6.5 eV for N Frenkel pairs [26]. Based on the combination of DFT and XRD data, it is inferred that the $V_{0.49}N_{0.51}$ layer contains V vacancies as well as N Frenkel pairs, causing the increase of the lattice parameter as observed experimentally.

The peak position of $V_{0.56}N_{0.44}$ at $2\theta = 44.25°$ results in a lattice parameter of 4.089 Å, Figure 4b. This experimental lattice parameter is in very good agreement with the DFT data, accommodating the N understoichiometry by N vacancies. The predicted lattice parameter, based on N vacancies, corresponds to 4.065 Å, and the deviation from the experimental value of 4.089 Å is < 0.6%, Figure 4c. Hence, the phase formation of $V_{0.56}N_{0.44}$ is governed by N vacancies based on the combination of ab initio and XRD data. Lattice parameters from ab initio calculations are 4.138 Å for $V_{0.49}N_{0.51}$, accommodating the N overstoichiometry by V vacancies and an N Frenkel pair, and 4.065 Å for $V_{0.56}N_{0.44}$, accommodating the N understoichiometry by N vacancies (-1.7(6)% strain at the $V_{0.49}N_{0.51}/V_{0.56}N_{0.44}$ interface). Corresponding experimental lattice parameters are 4.159 and 4.089 Å, respectively (1.6(8)% interfacial strain).

2.4 | Epitaxial Growth

The structure of the VN bilayer has been further investigated by TEM, as shown in Figure 5. An overview is shown in Figure 5a, and the individual $V_{0.49}N_{0.51}$ and $V_{0.56}N_{0.44}$ layers with thicknesses of ≈45 and ≈110 nm, respectively, can be clearly identified. The strong diffraction contrast differences originate from dislocations and local distortions. Compositional differences are highlighted by analysis of near-edge fine structures, Figure 5b, and the signal is in good agreement with data from VN [27]. Compared to the $V_{0.49}N_{0.51}$ layer, the N-K absorption edge of $V_{0.56}N_{0.44}$ reveals significant N deficiency at ≈410 eV. The second peak of the corresponding N-K edge slightly broadens and decreases in intensity, which can be explained by the formation of N vacancies [28]. Heteroepitaxial growth of $V_{0.49}N_{0.51}$ on the MgO(001) substrate is demonstrated with the high-resolution TEM image in Figure 5c, and individual diffractograms were obtained by fast Fourier transformations, Figure 5d and Figure 5e. The roughness of the MgO/$V_{0.49}N_{0.51}$ interface is on the order of 2 nm. A similar interface roughness has been reported for epitaxial growth of VN(111) on MgO(111) and explained by surface defects of commercially polished substrates [29]. Moreover, the high-resolution TEM image in Figure 5f and fast Fourier transformations in Figure 5g,h emphasize that the N-deficient $V_{0.56}N_{0.44}$ layer grows homoepitaxially on $V_{0.49}N_{0.51}$. Consequently, a single crystalline VN bilayer has been grown on MgO(001) at 400°C.

2.5 | Defect Structure and Local Strain Formation

The defect structure of the VN bilayer was investigated by a series of high-resolution TEM images (Figure 6). While recently the dislocation core structures have been studied for TiN single crystals [7], the present analyses focus on the evolution of the dislocation density within the VN bilayer. The highest dislocation density of ≈0.20 nm^{-2} is formed at the MgO/$V_{0.49}N_{0.51}$ interface and reduced to ≈0.10 nm^{-2} within $V_{0.49}N_{0.51}$ at a distance of ≈10 nm with respect to the MgO substrate, Figure 6b,c. The density of dislocations decreases to ≈0.04 nm^{-2} at the $V_{0.49}N_{0.51}/V_{0.56}N_{0.44}$ interface, Figure 6d, and < 0.01 nm^{-2} within the $V_{0.56}N_{0.44}$ layer at a distance of ≈35 nm from the $V_{0.49}N_{0.51}/V_{0.56}N_{0.44}$ interface (corresponding to a distance of ≈80 nm from the MgO/$V_{0.49}N_{0.51}$ interface), Figure 6e,f. Hence, the dislocation density varies by two orders of magnitude. Close to the surface of the bilayer, the dislocation density increases again to ≈0.03 nm^{-2}, Figure 6g, most likely related to surface oxidation, since a depth profile from time-of-flight elastic recoil detection analysis (not shown) provided evidence for significant O incorporation at the surface.

The linear density of misfit dislocations N can be estimated using the formula $N = \varepsilon/b$, where the strain ε is derived from XRD data. The Burgers vector b corresponds to $b = a/\sqrt{2}$ for edge dislocations, and a corresponds to the lattice parameter, also based on XRD data. Even when considering both strains of −0.9(5)% at the MgO/$V_{0.49}N_{0.51}$ interface as well as −1.7(6)% at the $V_{0.49}N_{0.51}/V_{0.56}N_{0.44}$ interface, a dislocation density of 0.09 nm^{-1} is estimated. Thus, the estimation provides evidence that interfacial misfit dislocations account only for a minor fraction of the observed high dislocation density. We propose that the majority of dislocations actually originates from the evolution of point defects into line defects. The mechanism of vacancy-driven dislocation multiplication has been widely observed in ionic crystals [30]. One key mechanism is the activation of the Bardeen-Herring source, which is a climb-dependent dislocation multiplication source. Another origin of a high dislocation density may be through the arrangement of vacancies, which has been recently proposed for overstoichiometric HfN [31].

The distribution of dislocations is further emphasized in Figure 7, and images of $V_{0.49}N_{0.51}$ in Figure 7a,b were obtained in a double-beam condition. While edge dislocations are evident in $V_{0.49}N_{0.51}$, a stacking fault is observed in $V_{0.56}N_{0.44}$, Figure 7c. Bright-field/dark-field (BF/DF) imaging reveals that the defect structure of the $V_{0.56}N_{0.44}$ layer primarily consists of threading dislocations and stacking faults. In contrast, threading dislocations in the $V_{0.49}N_{0.51}$ layer are indistinguishable in BF/DF imaging due to the excessively high dislocation density. Further high-resolution TEM observations confirmed the presence of a high density of $1/2a[110]$ full edge dislocations in this region.

The evolution of dislocation density as a function of the distance from the MgO/$V_{0.49}N_{0.51}$ interface is summarized in Figure 8 together with lattice parameters from XRD data. It is evident that the reduction of the dislocation density in $V_{0.49}N_{0.51}$ is correlated with the formation of V vacancies and N Frenkel pairs as inferred from DFT and XRD data. The $V_{0.56}N_{0.44}$ layer with N vacancies exhibits a two orders of magnitude lower dislocation density. Simultaneously, the lattice parameter is reduced from 4.199 Å for the MgO substrate to 4.159 Å for $V_{0.49}N_{0.51}$ and 4.089 Å for $V_{0.56}N_{0.44}$. Dislocations are predominantly formed in the entire ≈45 nm $V_{0.49}N_{0.51}$ layer. Thus, the evolution of the dislocation density in the VN bilayer is correlated with the N concentration.

21967350, 0, Downloaded from https://advanced.onlinelibrary.wiley.com/doi/10.1002/admi.202500774 by Universitatsbibliothek RWTH Aachen University, Wiley Online Library on [12/01/2026]. See the Terms and Conditions (https://onlinelibrary.wiley.com/terms-and-conditions) on Wiley Online Library for rules of use; OA articles are governed by the applicable Creative Commons License

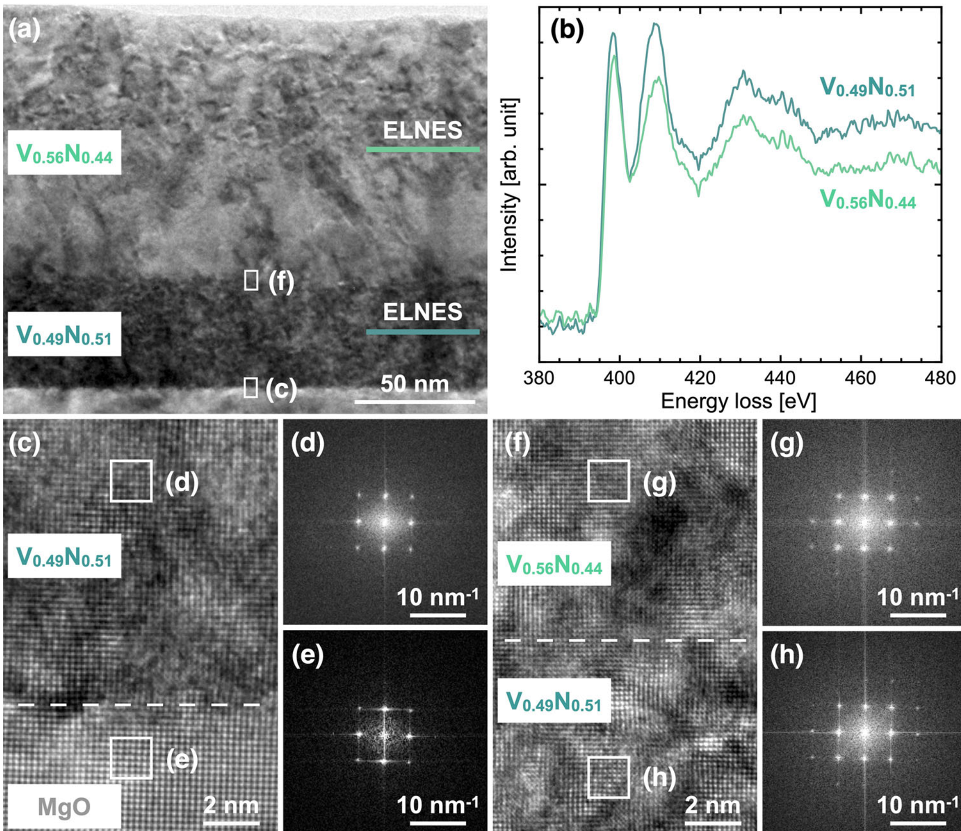

FIGURE 5 | Electron microscopy-based structural analysis of the VN bilayer. (a) Overview TEM image and a Pt protection layer can be seen at the top of the image. (b) N signal of electron loss near edge structure (ELNES) spectra from $V_{0.49}N_{0.51}$ and $V_{0.56}N_{0.44}$. The regions of the line scans are indicated in (a). (c) High-resolution TEM image of the $MgO/V_{0.49}N_{0.51}$ interface as well as fast Fourier transformations for (d) $V_{0.49}N_{0.51}$ and (e) MgO. Corresponding regions are indicated in (a) and (c). (f) High-resolution TEM image of the $V_{0.49}N_{0.51}/V_{0.56}N_{0.44}$ interface as well as fast Fourier transformations for (g) $V_{0.56}N_{0.44}$ and (h) $V_{0.49}N_{0.51}$. Corresponding regions are indicated in (a) and (f). Interfaces are emphasized by dashed lines.

Local strain fields with respect to the MgO substrate have been determined using geometrical phase analysis (GPA) from different regions of the VN bilayer, as indicated in Figure 9a. The MgO substrate was chosen as a reference from a region free of distortions, located ≈15 nm below the $MgO/V_{0.49}N_{0.51}$ interface, Figure 9b. High-resolution TEM images are shown together with the strain field in an out-of-plane direction (ε_{yy}) in Figure 9c–e. The critical thickness of 2-3 nm was found for the onset of strain relaxation in the case of VN/TiN superlattices [32]. However, at the $MgO/V_{0.49}N_{0.51}$ interface, strains with absolute values of > 10% are formed locally at dislocations, Figure 9c. At the $V_{0.49}N_{0.51}/V_{0.56}N_{0.44}$ interface, strains of -1.8 ± 0.6% and -1.9 ± 0.2% are obtained from dislocation-free regions of $V_{0.49}N_{0.51}$ and $V_{0.56}N_{0.44}$, respectively, Figure 9d. The very similar strain level may be understood by the gradient of the composition over ≈10 nm, as determined by APT, Figure 3.

The dislocation density is significantly reduced in the $V_{0.56}N_{0.44}$ layer, Figure 8, and the local strain of −2.7 ± 0.2% is obtained from line profile integration, Figure 9e, at a distance from the $MgO/V_{0.49}N_{0.51}$ interface of approximately 80-95 nm. This −2.7% mismatch of $V_{0.56}N_{0.44}$ with respect to the MgO substrate is in very good agreement with −2.6(2)% from XRD data. Comparing these values to the strain of −3.1(9)%, predicted by DFT and shown in Figure 4c, it is evident that the $V_{0.56}N_{0.44}$ layer is relaxed, see Figure 9e.

2.6 | Mechanical Properties

The elastic modulus and hardness of the VN bilayer film were assessed with nanoindentation, which is challenged by the relatively small thickness of ≈155 nm. For polycrystalline TiN films, the hardness could be reliably measured without contributions from the steel substrate, when the contact depth was up to 10% of the film thickness [33]. Significantly lower contact depths are required for measurements of the elastic modulus due to strain fields, which affect a larger volume than the plastic zone [33]. However, when reducing the contact depth, the indentation size effect has to be considered. Higher hardness values are measured for smaller contact depths, since gradients of plastic shear are associated with the storage of geometrically necessary dislocations [34]. Therefore, a contact depth range of 31–38 nm was chosen on purpose for nanoindentation of the VN bilayer, corresponding to 20–25% of the film thickness. While the measurement of mechanical properties is likely affected by a contribution from the MgO substrate, this contact depth range enables comparison of the mechanical properties to previous works on epitaxial VN films with maximum penetration depths of 30–40 nm [8, 9].

The VN bilayer exhibits an elastic modulus of 433 ± 19 GPa, slightly higher than the value of 400 ± 25 GPa for epitaxial $V_{0.51}N_{0.49}$ and in a similar range as 444 ± 24 GPa for $V_{0.56}N_{0.44}$

21967350, 0, Downloaded from https://advanced.onlinelibrary.wiley.com/doi/10.1002/admi.202500774 by Universitätsbibliothek RWTH Aachen University, Wiley Online Library on [12/01/2026]. See the Terms and Conditions (https://onlinelibrary.wiley.com/terms-and-conditions) on Wiley Online Library for rules of use; OA articles are governed by the applicable Creative Commons License

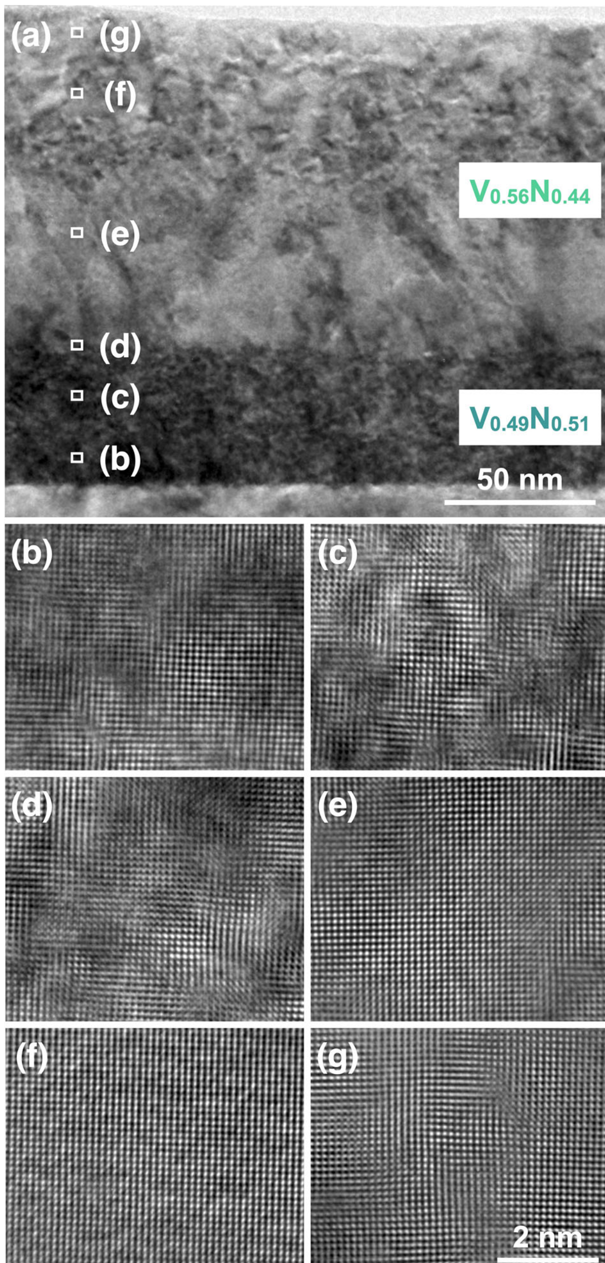

FIGURE 6 | Electron microscopy-based analysis of dislocation density. (a) Overview TEM image. (b–g) High-resolution TEM images from different regions, corresponding to different film thicknesses of the VN bilayer, as indicated in (a).

[9]. The hardness of the VN bilayer is 23.5 ± 0.9 GPa, which is ≈68% or ≈37% higher than the hardness of epitaxial $V_{0.50}N_{0.50}$ (14.0 ± 0.8 GPa) or $V_{0.56}N_{0.44}$ (17.1 ± 0.8 GPa), respectively [8]. We would like to emphasize that the mechanical properties of the VN bilayer are lower bound values due to the likely contribution of the MgO substrate with elastic modulus and hardness values in the ranges of 290–320 GPa and 9–13 GPa, respectively [35, 36]. Thus, it can be learned that the layered architecture of the VN bilayer with well-defined strained interfaces and two orders of magnitude variations in dislocation density is beneficial for the mechanical properties, in particular, the hardness is enhanced by up to > 60%.

3 | Conclusion

A single crystalline VN(001) bilayer has been grown epitaxially on MgO(001) by reactive HPPMS at 400°C in an industrial-scale deposition system. The individual layers were ≈45 nm of $V_{0.49}N_{0.51}$ and ≈110 nm of $V_{0.56}N_{0.44}$, and it is demonstrated that the defect structure and interfacial strain are governed by the N concentration. Based on the lattice mismatch between MgO and $V_{0.49}N_{0.51}$, an interfacial strain of −2.3(1)% is expected at the MgO/$V_{0.49}N_{0.51}$ interface. From DFT, XRD, and TEM data, it is inferred that the $V_{0.49}N_{0.51}$ layer exhibits V vacancies, N Frenkel pairs, and a dislocation density of ≈0.20 nm^{-2}, causing an interfacial strain of −1.4(5)% at the MgO/$V_{0.49}N_{0.51}$ interface. The phase formation of $V_{0.56}N_{0.44}$ is governed by N vacancies, and the dislocation density is reduced to ≈0.04 nm^{-2} at the $V_{0.49}N_{0.51}$/$V_{0.56}N_{0.44}$ interface and to < 0.01 nm^{-2} within the $V_{0.56}N_{0.44}$ layer at a distance of ≈35 nm from the interface. Ab initio data provide an expected strain of −1.7(6)%, at the $V_{0.49}N_{0.51}$/$V_{0.56}N_{0.44}$ interface, and are in very good agreement with the experimental interfacial strain of −1.6(8)%. Based on the here presented findings, it is evident that control of the N concentration allows for the design of layered architectures with well-defined strained interfaces and two orders of magnitude variations in dislocation density. Finally, the employment of only one transition metal is chemically simple and therefore, from a recycling point of view, also more sustainable than combining different transition metals as commonly done in layered architectures, including superlattices.

4 | Methods

4.1 | Thin Film Synthesis

VN bilayer films were grown on 10×10 mm MgO(001) as well as 15 × 15 mm glassy C substrates in a CemeCon CC800/9 deposition system. The substrates were clamped on a substrate holder, facing a rectangular V target (500 × 88 × 10 mm, 99.9% purity, Sindlhauser Materials GmbH) at a target-to-substrate distance of 10 cm. The deposition chamber was evacuated, and the substrate temperature was controlled with radiation heaters, located at the chamber walls (P = 4.5 kW) as well as in the center of the chamber (P = 1.5 kW). The temperature of 400 ± 5°C was achieved at the substrate holder and monitored with a thermocouple (NiCr-Ni, K type). After two hours of heating, the base pressure at the deposition temperature was < 2×10^{-4} Pa.

Bilayers were grown reactively through different gas supply systems of N_2 (purity 6.0) as schematically shown in Figure 1. The first layer with a nominal thickness of 50 nm was intended to be overstoichiometric (N concentration > 50 at.%); hence, N_2 was provided through the central gas inlet of the chamber [23]. A gas mixture with flows of 200 sccm Ar and 50 sccm N_2 was employed, resulting in a N_2 partial pressure of 0.10 Pa and a deposition pressure of 0.47 Pa. The second layer with a nominal thickness of 100 nm was intended to be understoichiometric (N concentration < 50 at.%), and a composition gradient was achieved by introducing N_2 through an inlet placed at the 88 mm wide end of the target (gas shower) [23]. The Ar flow was also 200 sccm, while the N_2 flow was 10 sccm, resulting in a N_2 partial pressure of 0.02 Pa and a deposition pressure of 0.39 Pa. The

21967350, 0, Downloaded from https://advanced.onlinelibrary.wiley.com/doi/10.1002/admi.202500774 by Universitatsbibliothek RWTH Aachen University, Wiley Online Library on [12/01/2026]. See the Terms and Conditions (https://onlinelibrary.wiley.com/terms-and-conditions) on Wiley Online Library for rules of use; OA articles are governed by the applicable Creative Commons License

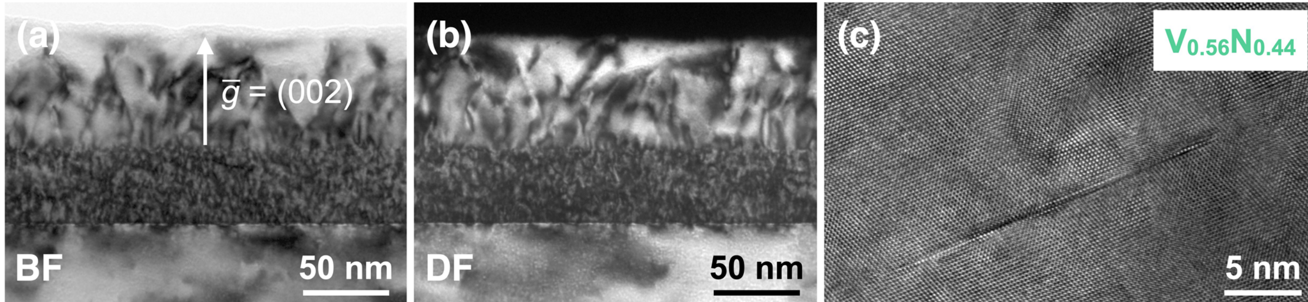

FIGURE 7 | Dislocation distribution and stacking fault formation. The overview of the VN bilayer, obtained in double-beam condition, is shown as bright field (BF) in (a) and dark field (DF) in (b). (c) Stacking fault, observed at <110> viewing direction in $V_{0.56}N_{0.44}$.

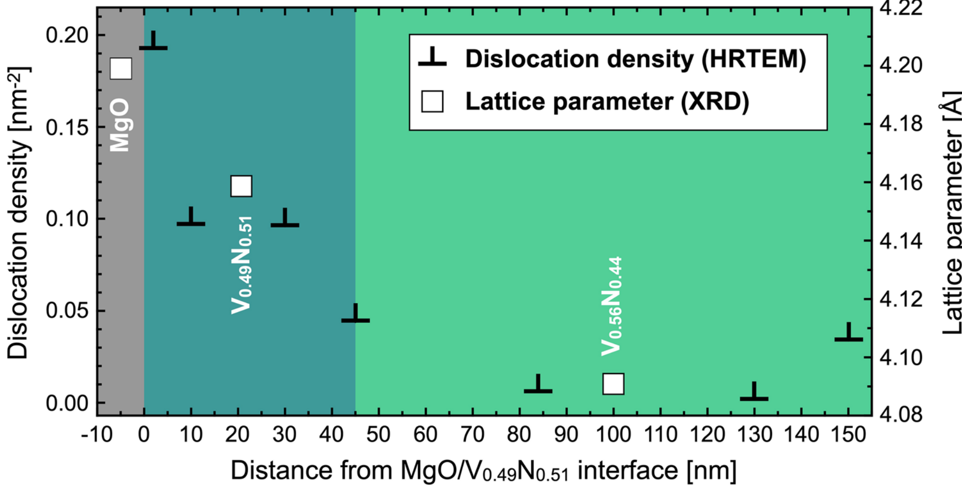

FIGURE 8 | Dislocation density as a function of the distance from the $MgO/V_{0.49}N_{0.51}$ interface based on high-resolution TEM (HRTEM) data (left axis). Lattice parameters of the MgO substrate, as well as $V_{0.49}N_{0.51}$ and $V_{0.56}N_{0.44}$ from XRD analysis, Figure 4c, are also included (right axis).

distance of the substrates from the gas shower inlet was in the range of ≈8 to ≈20 cm.

Both layers were synthesized by HPPMS with a Melec SIPP2000USB-10-500-S power supply, and the pulse on- and off-times were 50 and 1950 µs, respectively, corresponding to a frequency of 500 Hz and a duty cycle of 2.5%. The time-average power of 1.5 kW was applied, and the waveforms of target voltage and current were monitored with a Tektronix TDS 3014B oscilloscope. The substrate holder was at floating potential, and the deposition time of the first VN layer, grown with the central gas inlet, was 190 s. Afterward the plasma was stopped, N_2 was supplied through the gas shower, and the second VN layer was grown for 360 s. Since these two layers exhibited thicknesses of ≈45 nm (central gas inlet) and ≈110 nm (gas shower), actual deposition rates were 2.4 Å s^{-1} and 3.1 Å s^{-1}, respectively. The venting temperature was < 70°C to minimize surface oxidation [37].

4.2 | Ion Beam Analysis

VN bilayer films, grown on glassy C, were characterized by RBS at the Tandem Laboratory of Uppsala University [38]. A primary ion beam of $^{4}He^{+}$ with 2 MeV energy was used, and backscattered ions were detected at a scattering angle of 170°. Data analysis was done with SIMNRA [39]. The statistical uncertainty was 3–4 and 2-3% relative of the deduced values for $V_{0.49}N_{0.51}$ and $V_{0.56}N_{0.44}$, respectively. In addition, depth profiles of the films, grown on MgO, were acquired with time-of-flight elastic recoil detection analysis to investigate the O impurity content. Primary ions $^{127}I^{8+}$ with 36 MeV energy were used, and time-energy coincidence spectra were obtained with a combination of thin C foils as well as a gas detector [40].

4.3 | Atom Probe Tomography

The nanoscale composition of the VN bilayer was characterized spatially resolved with APT using a CAMECA LEAP 4000 X HR. Field evaporation was assisted thermally with an ultraviolet laser, operated at a pulse frequency of 200 kHz, and the base temperature as well as detection rate were 60 K and 0.5%, respectively. Since the measurement accuracy is strongly dependent on the electric field strength, a low laser pulse energy of 10 pJ was employed. Thereby, the higher electric field strength enhances the measurement accuracy as recently demonstrated for the related systems TiN and CrN [41, 42].

21967350, 0, Downloaded from https://advanced.onlinelibrary.wiley.com/doi/10.1002/admi.202500774 by Universitatsbibliothek RWTH Aachen University, Wiley Online Library on [12/01/2026]. See the Terms and Conditions (https://onlinelibrary.wiley.com/terms-and-conditions) on Wiley Online Library for rules of use; OA articles are governed by the applicable Creative Commons License

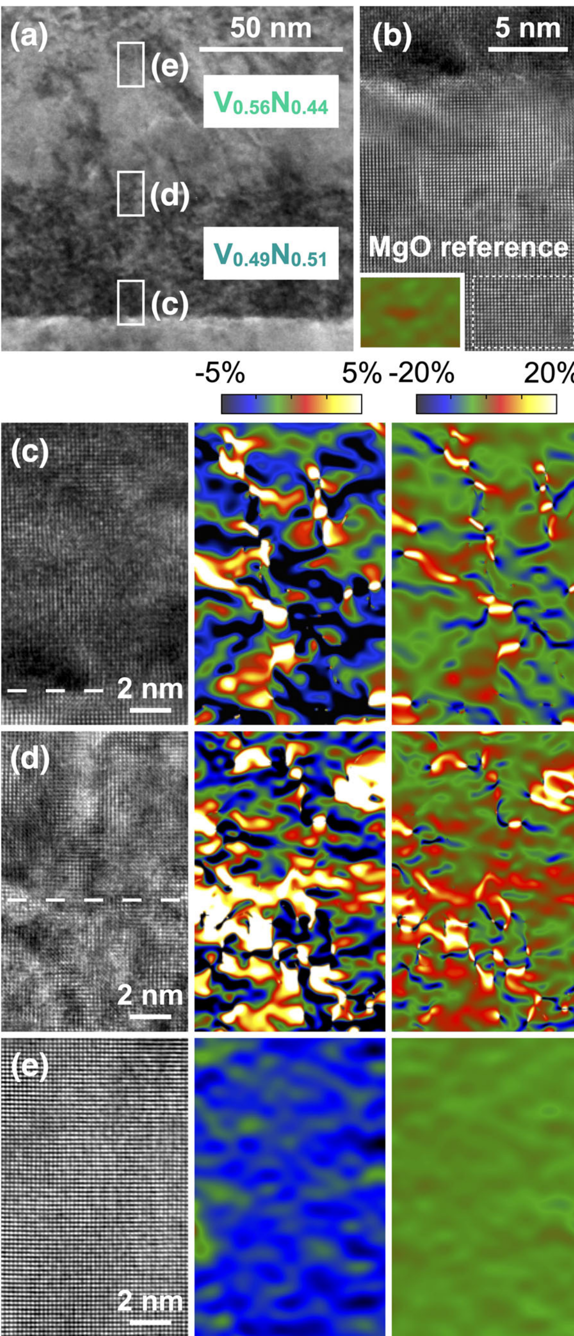

FIGURE 9 | Electron microscopy-based analysis of local strain fields. (a) Overview TEM image. (b) Region of the MgO reference for strain analysis, located ≈15 nm from the MgO/$V_{0.49}N_{0.51}$ interface. High-resolution TEM images and corresponding strain fields are shown for (c) the MgO/$V_{0.49}N_{0.51}$ interface, (d) the $V_{0.49}N_{0.51}$/$V_{0.56}N_{0.44}$ interface, and (e) the $V_{0.56}N_{0.44}$ layer. Strain fields are provided with two color scales from −5 to +5% as well as −20 to +20%. The strain field of the MgO reference is shown with the color scale from −20 to +20%. Interfaces are emphasized by dashed lines.

Atom probe specimens were prepared by focused ion beam techniques in a FEI Helios Nanolab 660 dual-beam microscope, using Ga^+ ions at 30 kV. A plan-view lift-out (see supporting information of previous work [43]) was done due to the limited thickness of the bilayer and to avoid material loss during the sharpening of the specimens to a needle-shaped geometry. Final specimen preparation was done at 5 kV to reduce the Ga contamination, and a specimen with 30 nm radius at the apex and 12° shank angle was obtained. Data analysis was carried out with AP Suite 6.1, and the shank angle protocol was used for reconstruction.

4.4 | X-ray Diffraction

Phase formation was studied with a Siemens D5000 diffractometer. Cu Kα radiation ($\lambda = 1.54$ Å) was used for XRD at a voltage of 40 kV and a current of 40 mA. The 2θ range from 40 to 46° was scanned with a step size of 0.05° and dwell time of 2 s, while the X-ray source and detector were coupled in θ–2θ scans. Thereby, the (200) lattice planes were studied, and lattice parameters from the VN bilayer as well as the MgO substrate were obtained. Peak deconvolution was carried out with the Profex program [44], employing Pseudo-Voigt fitting functions.

4.5 | Transmission Electron Microscopy

A field emission (scanning) transmission electron microscope (JEOL 2100F), equipped with an image-side spherical aberration corrector, was used and can achieve a resolution of 1.2 Å at 200 kV. The aberration coefficients were tuned to be sufficiently small (C_S = 0 µm), and all high-resolution TEM images were taken under slight over-focus conditions. Moreover, electron energy loss spectroscopy was employed, and spectrum images were acquired in the scanning transmission electron microscopy mode using a dispersion of 0.2 eV per channel, a collection semi-angle of 10 mrad, and a convergence semi-angle of 2.5 mrad. The images were aligned to the first N-K peak and processed in Digital Micrograph software. The dislocation density was obtained from high-resolution images according to $\rho = N/A$, where ρ is the dislocation density, N is the number of dislocations, A is the area. The strain field was calculated on the C_S-corrected high-resolution TEM images using the GPA method. According to the GPA algorithm, the lattice strain in the out-of-plane direction (ε_{yy}) can be obtained by selecting two non-collinear Bragg vectors $\left(\vec{g}_1 = (200)\ \textit{and}\ \vec{g}_1 = (200)\right)$ in the power spectrum generated from a high-resolution TEM image.

Thin lamellae for TEM investigations were also prepared using the dual-beam microscope mentioned above. A platinum protection layer with length, width and height of 8.0, 1.5 and 1.5 µm, respectively, was applied on the surface of the VN bilayer. The lift-out consisted of approximately 1.5 µm of the MgO substrate, the VN bilayer, as well as the protection layer. Preliminary thinning of a window with a width of ≈2.5 µm to ≈60 nm lamella thickness was done at 30 kV with currents of 0.79 as well as 0.23 nA, while the final thinning to ≈20 nm was carried out at 5 kV using currents of 41 as well as 15 pA. Energy dispersive X-ray spectroscopy was done in the TEM, and no Ga impurities were found in the lamellae (data not shown). Besides conventional lift-outs in the <100> viewing direction, an additional lift-out was done in the <110> viewing direction.

21967350, 0, Downloaded from https://advanced.onlinelibrary.wiley.com/doi/10.1002/admi.202500774 by Universitatsbibliothek RWTH Aachen University, Wiley Online Library on [12/01/2026]. See the Terms and Conditions (https://onlinelibrary.wiley.com/terms-and-conditions) on Wiley Online Library for rules of use; OA articles are governed by the applicable Creative Commons License

4.6 | Nanoindentation

Elastic modulus and hardness were evaluated with quasistatic nanoindentation using a Hysitron TI-900 TriboIndenter. In total, 50 indents were done at the VN bilayer in load-controlled measurement mode with loads of 1.0 and 1.2 mN (25 indents for each load). The resulting contact depths were in the range of 31–38 nm, corresponding to 20–25% of the film thickness. While a contribution of the MgO(001) substrate to the measured mechanical properties has to be expected, these relatively large contact depths were chosen on purpose for comparison with previous works on epitaxial VN films [8, 9] and to avoid the indentation size effect. A new diamond probe with Berkovich geometry and 100 nm nominal radius was employed, since blunting of the probe results in overestimation of the hardness due to an enhanced indentation size effect [33]. Individual load-displacement curves were evaluated according to the method from Oliver and Pharr [45]. Measured indentation modulus values were converted to the elastic modulus using a Poisson ratio of 0.296 for $V_{0.5}N_{0.5}$ [9] as well as a Poisson ratio of 0.07 and an elastic modulus of 1140 GPa for the diamond probe. The area function of the probe was determined with a fused silica reference sample.

4.7 | Modeling

Lattice parameters of cubic VN (space group $Fm\bar{3}m$) as a function of N concentration were predicted at 0 K by DFT ab initio calculations [46] as implemented within Quantum ESPRESSO [47, 48] in version 7.2. Electron exchange-correlation was obtained from the general gradient approximation in Perdew, Burke, and Ernzerhof (PBE) parametrization [49].

Besides the stoichiometric configuration, 2 × 2 × 2 supercells with 56–64 atoms were used with either metal or N vacancies at random positions by utilization of a special quasirandom structure generator [50]. N concentrations were 42.9, 44.8, 46.7, 48.4, 50.0, 51.6, and 53.3 at.% (cell configurations: $V_{32}N_{24}$, $V_{32}N_{26}$, $V_{32}N_{28}$, $V_{32}N_{30}$, $V_{32}N_{32}$, $V_{30}N_{32}$ and $V_{28}N_{32}$). Elements of the investigated structures were described by pseudopotentials from the Standard Solid-State Pseudopotentials (SSSP) PBE Precision package, version 1.3.0 [51, 52]. All the calculations were facilitated via the Atomic Simulation Environment [53].

Kinetic cut-off energies for wavefunctions and charge density were chosen as 80 Ry and 320 Ry, respectively, based on values for V and N provided by the SSSP PBE Precision version 1.3.0 cut-off tables [51, 52]. Sampling of the Brillouin zone was done by Γ-centered Monkhorst-Pack mesh [54] with k-points spacing 0.15 $Å^{-1}$ for which convergence tests suggested that the structures were well-converged. Convergence thresholds were set to 10^{-5} Ry and 10^{-4} Ry $Bohr^{-1}$ for the total energy and forces, respectively. All calculations herein were performed without consideration of spin polarization.

Cubic VN is dynamically unstable and transforms into a tetragonal structure (space group $P\bar{4}_2m$) at temperatures below 250 K [55, 56]. The calculations were carried out at 0 K, and all structures initially underwent full-cell geometry optimization, in which the Bravais lattice was fixed, and volume was allowed to change. For these optimizations, Gaussian smearing with a spread of 0.015 Ry was used for Brillouin-zone integration. The obtained ground state geometries were then subjected to additional single-point calculations using optimized tetrahedron method [57] to obtain accurate total energies.

To model possibly present N Frenkel pairs within the structures and investigate their influence on the lattice, twelve interstitial configurations were considered for the $V_{32}N_{32}$ model; four having the interstitial atom close to the corresponding vacancy and eight placing the interstitial atom beyond V atoms closest to the corresponding vacancy. Out of these, only four Frenkel pair configurations were found to persist – all of them being located further from the corresponding vacancy – and the other configurations exhibited interstitial-vacancy recombination. The persistent configurations were then also tested for $V_{30}N_{32}$ and $V_{28}N_{32}$ systems, where they were found to mostly persist as well (three out of four for $V_{30}N_{32}$ and two out of four for $V_{28}N_{32}$). When introducing an additional vacancy at the N site, the Frenkel pair recombined spontaneously. Similarly, eight configurations of $V_{32}N_{32}$ with a V Frenkel pair were tested, all having the interstitial atom located beyond the N atoms closest to the corresponding V vacancy. Four out of these eight configurations were found to persist. Testing of the V Frenkel pairs for $V_{30}N_{32}$ and $V_{28}N_{32}$ led in all cases to recombination, suggesting that the presence of any additional V vacancy destabilizes the V Frenkel pair in a similar manner to N Frenkel pairs.

Acknowledgements

The authors are grateful for financial support from Deutsche Forschungsgemeinschaft (DFG) within the project 515702322 (HA 9139/1-1, SCHN 735/50-1). The provision of computing resources granted by the Jülich-Aachen Research Alliance (JARA) HPC section at the IT Center of RWTH Aachen University within the project jara0151 is acknowledged. Zhuo Chen and Zaoli Zhang acknowledge financial support from the Austrian Science Fund (FWF): P-33696. Accelerator operation at Uppsala University has been supported by the Swedish Research Council (VR-RFI) within grant agreement #2019-00191. Lastly, the authors gratefully acknowledge the computing time provided by the NHR Center NHR4CES at RWTH Aachen University (project number p0020883). This center is funded by the Federal Ministry of Education and Research, and the state governments participating based on the resolutions of the GWK for national high-performance computing at universities (https://nhr-verein.de/en/our-partners).

Conflicts of Interest

The authors declare no conflict of interest.

Data Availability Statement

The data that support the findings of this study are available from the corresponding author upon reasonable request.

References

1. H. Holleck, *Metastable Coatings – Prediction of Composition and Structure*, Surface Engineering: Science and Technology, (Eds.: A. Kumar, Y.-W. Chung, and J. J. Moore), *Metastable Coatings – Prediction of Composition and Structure*, (The Minerals, Metals and Materials Society, 1999): 207–218.

21967350, 0, Downloaded from https://advanced.onlinelibrary.wiley.com/doi/10.1002/admi.202500774 by Universitatsbibliothek RWTH Aachen University, Wiley Online Library on [12/01/2026]. See the Terms and Conditions (https://onlinelibrary.wiley.com/terms-and-conditions) on Wiley Online Library for rules of use; OA articles are governed by the applicable Creative Commons License

2. E. Friederich and L. Sittig, “Herstellung und Eigenschaften von Nitriden,” *Zeitschrift für Anorganische und Allgemeine Chemie* 143 (1925): 293–320, https://doi.org/10.1002/zaac.19251430121.

3. H. J. Spitzer, “Relationship Between Substrate Temperature, Structure, and Superconducting Properties of Reactively Sputtered Niobium Nitride Thin Films,” *Journal of Vacuum Science and Technology* 9 (1972): 333–336, https://doi.org/10.1116/1.1316599.

4. B. O. Johansson, J. E. Sundgren, J. E. Greene, A. Rockett, and S. A. Barnett, “Growth and Properties of Single Crystal TiN Films Deposited by Reactive Magnetron Sputtering,” *Journal of Vacuum Science and Technology A* 3 (1985): 303–307, https://doi.org/10.1116/1.573255.

5. C.-S. Shin, D. Gall, N. Hellgren, J. Patscheider, I. Petrov, and J. E. Greene, “Vacancy Hardening in Single-Crystal TiN_x(001) Layers,” *Journal of Applied Physics* 93 (2003): 6025–6028, https://doi.org/10.1063/1.1568521.

6. S.-H. Jhi, S. G. Louie, M. L. Cohen, and J. Ihm, “Vacancy Hardening and Softening in Transition Metal Carbides and Nitrides,” *Physical Review Letters* 86 (2001): 3348–3351, https://doi.org/10.1103/PhysRevLett.86.3348.

7. J. Salamania, D. G. Sangiovanni, A. Kraych, et al., “Elucidating Dislocation Core Structures in Titanium Nitride Through High-Resolution Imaging and Atomistic Simulations,” *Master & Design* 224 (2022): 111327, https://doi.org/10.1016/j.matdes.2022.111327.

8. A.-B. Mei, H. Kindlund, E. Broitman, et al., “Adaptive Hard and Tough Mechanical Response in Single-Crystal B1 VN_x Ceramics via Control of Anion Vacancies,” *Acta Materialia* 192 (2020): 78–88, https://doi.org/10.1016/j.actamat.2020.03.037.

9. S. Karimi Aghda, D. Bogdanovski, L. Löfler, et al., “Valence Electron Concentration- and N Vacancy-Induced Elasticity in Cubic Early Transition Metal Nitrides,” *Acta Materialia* 255 (2023): 119078, https://doi.org/10.1016/j.actamat.2023.119078.

10. U. Helmersson, S. Todorova, S. A. Barnett, J.-E. Sundgren, L. C. Markert, and J. E. Greene, “Growth of Single-Crystal TiN/VN Strained-Layer Superlattices with Extremely High Mechanical Hardness,” *Journal of Applied Physics* 62 (1987): 481–484, https://doi.org/10.1063/1.339770.

11. Z. Chen, Y. Zheng, Y. Huang, et al., “Atomic-Scale Understanding of the Structural Evolution in TiN/AlN Superlattice During Nanoindentation – Part 2: Strengthening,” *Acta Materialia* 234 (2022): 118009, https://doi.org/10.1016/j.actamat.2022.118009.

12. W. J. Meng, G. L. Eesley, and K. A. Svinarich, “Structural and Elastic Properties of zirconium Nitride–Aluminum Nitride Multilayers,” *Physical Review B* 42 (1990): 4881–4884, https://doi.org/10.1103/PhysRevB.42.4881.

13. M. Shinn, L. Hultman, and S. A. Barnett, “Growth, Structure, and Microhardness of Epitaxial TiN/NbN Superlattices,” *Journal of Materials Research* 7 (1992): 901–911, https://doi.org/10.1557/JMR.1992.0901.

14. M. Schlögl, B. Mayer, J. Paulitsch, and P. H. Mayrhofer, “Influence of CrN and AlN Layer Thicknesses on Structure and Mechanical Properties of CrN/AlN Superlattices,” *Thin Solid Films* 545 (2013): 375–379, https://doi.org/10.1016/j.tsf.2013.07.026.

15. R. Hahn, M. Bartosik, R. Soler, C. Kirchlechner, G. Dehm, and P. H. Mayrhofer, “Superlattice Effect for Enhanced Fracture Toughness of Hard Coatings,” *Scripta Materialia* 124 (2016): 67–70, https://doi.org/10.1016/j.scriptamat.2016.06.030.

16. T. Wang, Y. Jin, L. Bai, and G. Zhang, “Structure and Properties of NbN/MoN Nano-Multilayer Coatings Deposited by Magnetron Sputtering,” *Journal of Alloys and Compounds* 729 (2017): 942–948, https://doi.org/10.1016/j.jallcom.2017.09.218.

17. J. Buchinger, N. Koutná, Z. Chen, et al., “Toughness Enhancement in TiN/WN Superlattice Thin Films,” *Acta Materialia* 172 (2019): 18–29, https://doi.org/10.1016/j.actamat.2019.04.028.

18. R. Hahn, N. Koutná, T. Wójcik, et al., “Mechanistic Study of Superlattice-Enabled High Toughness and Hardness in MoN/TaN Coatings,” *Communication Materials* 1 (2020): 62, https://doi.org/10.1038/s43246-020-00064-4.

19. Z. Zhang, R. Daniel, and C. Mitterer, “Atomic and Electronic Structures of a Transition Layer at the CrN/Cr Interface,” *Journal of Applied Physics* 110 (2011): 043524, https://doi.org/10.1063/1.3624772.

20. S. Evertz, J. Zálešák, M. Hans, et al., “Mapping Strain Across $Co_{80}Ta_7B_{13}$ /$Co_{62}Ta_6B_{32}$ Glassy Interfaces,” *Material & Design* 234 (2023): 112327, https://doi.org/10.1016/j.matdes.2023.112327.

21. M. Hans, J. M. Schneider, A. Matthews, and C. Mitterer, “Perspective on Pathways Towards Responsible Surface Engineering,” *Surf Coat Technol* 494 (2024): 131486, https://doi.org/10.1016/j.surfcoat.2024.131486.

22. V. Kouznetsov, K. Macák, J. M. Schneider, U. Helmersson, and I. Petrov, “A Novel Pulsed Magnetron Sputter Technique Utilizing Very High Target Power Densities,” *Surface and Coatings Technology* 122 (1999): 290–293, https://doi.org/10.1016/S0257-8972(99)00292-3.

23. M. to Baben, M. Hans, D. Primetzhofer, S. Evertz, H. Rueß, and J. M. Schneider, “Unprecedented Thermal Stability of Inherently Metastable Titanium Aluminum Nitride by Point Defect Engineering,” *Materials Research Letters* 5 (2017): 158–169, https://doi.org/10.1080/21663831.2016.1233914.

24. S. Berg, H.-O. Blom, T. Larsson, and C. Nender, “Modeling of Reactive Sputtering of Compound Materials,” *Journal of Vacuum Science and Technology A* 5 (1987): 202–207, https://doi.org/10.1116/1.574104.

25. B. Gault, D. W. Saxey, M. W. Ashton, et al., “Behavior of Molecules and Molecular Ions Near a Field Emitter,” *New Journal of Physics* 18 (2016): 033031, https://doi.org/10.1088/1367-2630/18/3/033031.

26. S. Karimi Aghda, D. Music, Y. Unutulmazsoy, et al., “Unravelling the Ion-Energy-Dependent Structure Evolution and its Implications for the Elastic Properties of (V,Al)N Thin Films,” *Acta Materialia* 214 (2021): 117003, https://doi.org/10.1016/j.actamat.2021.117003.

27. F. Hofer, P. Warbichler, A. Scott, R. Brydson, I. Galesic, and B. Kolbesen, “Electron Energy Loss Near Edge Structure on the Nitrogen K-Edge in Vanadium Nitrides,” *Journal of Microscopy* 204 (2001): 166–171, https://doi.org/10.1046/j.1365-2818.2001.00946.x.

28. Z. Zhang, H. Li, R. Daniel, C. Mitterer, and G. Dehm, “Insights Into the Atomic and Electronic Structure Triggered by Ordered Nitrogen Vacancies in CrN,” *Physics Review B* 87 (2013): 014104, https://doi.org/10.1103/PhysRevB.87.014104.

29. P. Lazar, B. Rashkova, J. Redinger, et al., “Interface Structure of Epitaxial (111) VN Films on (111) MgO Substrates,” *Thin Solid Films* 517 (2008): 1177–1181, https://doi.org/10.1016/j.tsf.2008.06.006.

30. J. P. Hirth and J. Lothe, *Theory of Dislocations*, 2nd edition. (Wiley, 1982).

31. M. Lorentzon, D. G. Sangiovanni, N. Takata, et al., “Metal-Like Ductility and High Hardness in Nitrogen-Rich HfN Thin Films by Point Defect Superstructuring,” *Communication Materials* 6 (2025): 46, https://doi.org/10.1038/s43246-025-00768-5.

32. L. Hultman, M. Shinn, P. B. Mirkarimi, and S. A. Barnett, “Characterization of Misfit Dislocations in Epitaxial (001)-Oriented TiN, NbN, VN, and (Ti,Nb)N Film Heterostructures by Transmission Electron Microscopy,” *Journal of Crystal Growth* 135 (1994): 309–317, https://doi.org/10.1016/0022-0248(94)90757-9.

33. S. J. Bull, “Microstructure and Indentation Response of TiN Coatings: The Effect of Measurement Method,” *Thin Solid Films* 688 (2019): 137452, https://doi.org/10.1016/j.tsf.2019.137452.

34. N. A. Fleck, G. M. Muller, M. F. Ashby, and J. W. Hutchinson, “Strain gradient Plasticity: Theory and Experiment,” *Acta Metallurgica et Materialia* 42 (1994): 475–487, https://doi.org/10.1016/0956-7151(94)90502-9.

35. H. Ljungcrantz, M. Odén, L. Hultman, J. E. Greene, and J.-E. Sundgren, “Nanoindentation Studies of Single-Crystal (001)-, (011)-, and (111)-Oriented TiN Layers on MgO,” *Journal Applied Physics* 80 (1996): 6725–6733, https://doi.org/10.1063/1.363799.

21967350, 0, Downloaded from https://advanced.onlinelibrary.wiley.com/doi/10.1002/admi.202500774 by Universitatsbibliothek RWTH Aachen University, Wiley Online Library on [12/01/2026]. See the Terms and Conditions (https://onlinelibrary.wiley.com/terms-and-conditions) on Wiley Online Library for rules of use; OA articles are governed by the applicable Creative Commons License

36. D. Cáceres, I. Vergara, R. González, and Y. Chen, “Nanoindentation on Nominally Pure and Doped MgO Crystals,” *Radiation Effects and Defects* 156 (2001): 39–43, https://doi.org/10.1080/10420150108216870.

37. G. Greczynski, S. Mráz, L. Hultman, and J. M. Schneider, “Venting Temperature Determines Surface Chemistry of Magnetron Sputtered TiN Films,” *Applied Physics Letters* 108 (2016): 041603, https://doi.org/10.1063/1.4940974.

38. P. Ström and D. Primetzhofer, “Ion Beam Tools for Nondestructive In-Situ and In-Operando Composition Analysis and Modification of Materials at the Tandem Laboratory in Uppsala,” *Journal of Instrumentation* 17 (2022): P04011, https://doi.org/10.1088/1748-0221/17/04/P04011.

39. M. Mayer, “SIMNRA, a Simulation Program for the Analysis of NRA, RBS and ERDA,” *American Institute of Physics Conference Proceedings* 475 (1999): 541–544, https://doi.org/10.1063/1.59188.

40. P. Ström, P. Petersson, M. Rubel, and G. Possnert, “A Combined Segmented Anode Gas Ionization Chamber and Time-of-Flight Detector for Heavy Ion Elastic Recoil Detection Analysis,” *Review of Scientific Instruments* 87 (2016): 103303, https://doi.org/10.1063/1.4963709.

41. M. Hans, M. Tkadletz, D. Primetzhofer, et al., “Is it Meaningful to Quantify Vacancy Concentrations of Nanolamellar (Ti,Al)N Thin Films Based on Laser-Assisted Atom Probe Data?,” *Surface and Coatings Technology* 473 (2023): 130020, https://doi.org/10.1016/j.surfcoat.2023.130020.

42. H. Waldl, M. Hans, M. Schiester, et al., “Decomposition of CrN Induced by laser-Assisted Atom Probe Tomography,” *Ultramicroscopy* 246 (2023): 113673, https://doi.org/10.1016/j.ultramic.2022.113673.

43. M. Hans, Z. Czigány, D. Neuß, et al., “Probing the Onset of Wurtzite Phase Formation in (V,Al)N Thin Films by Transmission Electron Microscopy and Atom Probe Tomography,” *Surface and Coatings Technology* 442 (2022): 128235, https://doi.org/10.1016/j.surfcoat.2022.128235.

44. N. Doebelin and R. Kleeberg, “Profex: A Graphical User Interface for the Rietveld Refinement Program BGMN,” *Journal of Applied Crystallography* 48 (2015): 1573–1580, https://doi.org/10.1107/S1600576715014685.

45. W. C. Oliver and G. M. Pharr, “An Improved Technique for Determining Hardness and Elastic Modulus Using Load and Displacement Sensing Indentation Experiments,” *Journal of Materials Research* 7 (1992): 1564–1583, https://doi.org/10.1557/JMR.1992.1564.

46. P. Hohenberg and W. Kohn, “Inhomogeneous Electron Gas,” *Physical Review* 136 (1964): B864–B871, https://doi.org/10.1103/PhysRev.136.B864.

47. P. Giannozzi, S. Baroni, N. Bonini, et al., “QUANTUM ESPRESSO: A Modular and Open-Source Software Project for Quantum Simulations of Materials,” *Journal of Physics: Condensed Matter* 21 (2009): 395502, https://doi.org/10.1088/0953-8984/21/39/395502.

48. P. Giannozzi, O. Andreussi, T. Brumme, et al., “Advanced Capabilities for Materials Modelling with QUANTUM ESPRESSO,” *Journal of Physics: Condensed Matter* 29 (2017): 465901, https://doi.org/10.1088/1361-648X/aa8f79.

49. J. P. Perdew, K. Burke, and M. Ernzerhof, “Generalized Gradient Approximation Made Simple,” *Physical Review Letters* 77 (1996): 3865–3868, https://doi.org/10.1103/PhysRevLett.77.3865.

50. D. Gehringer, M. Friák, and D. Holec, “Models of Configurationally-Complex Alloys Made Simple,” *Computer Physics Communications* 286 (2023): 108664, https://doi.org/10.1016/j.cpc.2023.108664.

51. G. Prandini, A. Marrazzo, I. E. Castelli, N. Mounet, and N. Marzari, “Precision and Efficiency in Solid-State Pseudopotential Calculations,” *npj Computational Materials* 4 (2018): 72, https://doi.org/10.1038/s41524-018-0127-2.

52. L. Talirz, S. Kumbhar, E. Passaro, et al., “Materials Cloud, a Platform for Open Computational Science,” *Scientific Data* 7 (2020): 299, https://doi.org/10.1038/s41597-020-00637-5.

53. A. H. Larsen, J. J. Mortensen, J. Blomqvist, et al., “The Atomic Simulation Environment – a Python Library for Working with Atoms,” *Journal of Physics: Condensed Matter* 29 (2017): 273002, https://doi.org/10.1088/1361-648X/aa680e.

54. H. J. Monkhorst and J. D. Pack, “Special Points for Brillouin-Zone Integrations,” *Physical Review B* 78 (1976): 1396, https://doi.org/10.1103/PhysRevB.13.5188.

55. F. Kubel, W. Lengauer, K. Yvon, K. Knorr, and A. Junod, “Structural Phase Transition at 205 K in Stoichiometric Vanadium Nitride,” *Physical Review B* 38 (1988): 12908–12912, https://doi.org/10.1103/PhysRevB.38.12908.

56. A. B. Mei, O. Hellman, N. Wireklint, et al., “Dynamic and Structural Stability of Cubic Vanadium Nitride,” *Physical Review B* 91 (2015): 054101, https://doi.org/10.1103/PhysRevB.91.054101.

57. M. Kawamura, Y. Gohda, and S. Tsuneyuki, “Improved Tetrahedron Method for the Brillouin-Zone Integration Applicable to Response Functions,” *Physical Review B* 89 (2014): 094515, https://doi.org/10.1103/PhysRevB.89.094515.

21967350, 0, Downloaded from https://advanced.onlinelibrary.wiley.com/doi/10.1002/admi.202500774 by Universitatsbibliothek RWTH Aachen University, Wiley Online Library on [12/01/2026]. See the Terms and Conditions (https://onlinelibrary.wiley.com/terms-and-conditions) on Wiley Online Library for rules of use; OA articles are governed by the applicable Creative Commons License